Nonlinear Diffusion vs. Wavelet Based Noise Reduction in CT Using Correlation Analysis

M. Mayer, A. Borsdorf, H. Köstler, J. Hornegger, and U. Rüde

Lehrstuhl für Mustererkennung & Lehrstuhl für Systemsimulation
Friedrich-Alexander Universität Erlangen-Nürnberg
Correspondence Email: `harald.koestler@informatik.uni-erlangen.de`

Abstract

We propose a new PDE based method for noise reduction in computed tomography (CT) using correlation analysis and compare it to a previously introduced wavelet based method. The arising nonlinear (an)isotropic PDEs are solved by an efficient multigrid solver.

Both approaches are based on the assumption that the data can be decomposed into information and temporally uncorrelated noise. In CT two spatially identical images can be generated by reconstructions from disjoint subsets of projection, e.g., by taking every other projection respectively. Our experimental results in 2D and 3D show that a noise reduction up to 66% can be achieved without noticable loss of image resolution. Additionally, a radiologist compared the visual quality of both methods with respect to noise and visibility of structures for real clinical data.

1 Introduction

Noise reduction in CT images gains more and more attention. It provides a possibility to increase the signal-to-noise ratio (SNR), hence giving more space for a further reduction of radiation dose.

Several methods for the reduction of noise in CT have been proposed [1, 2, 3], in most cases reducing noise in the projections before reconstruction. In contrast to this we focus on the reduction of noise in the reconstructed 2D slices or 3D volumes. Noise reduction in reconstructed CT datasets is not an easy task due to the difficult noise properties: after reconstruction the distribution of noise is unknown. Furthermore, noise is non-stationary and directed noise due to high attenuation along certain directions may be present.

In [4] we proposed a wavelet based denoising method for CT images. By separately reconstructing the odd and even numbered projections of a CT scan two sets of slices are obtained which include the same information but noise between the data is uncorrelated. By using correlation analysis in the wavelet domain combined with an orientation and position dependent noise estimation [5] only those wavelet coefficients containing image structure are kept for reconstruction of a noise suppressed image. In [6], the idea of this approach, e.g., using two data sets with uncorrelated noise, is picked up and transfered to the spatial domain, where we apply nonlinear isotropic diffusion filtering [7, 8]. Now, we extend it to the anisotropic case, compare it to the wavelets, and present results on clinical data.

An overview of the methodology is presented in Section 2. Section 3 summarizes the wavelet based approach. Then, we propose in Section 4 a new noise reduction method based on nonlinear (an)isotropic diffusion that tries to estimate the real image structure out of the correlations of two input datasets affected with uncorrelated noise. In Section 5 we compare the two methods with respect to noise reduction and edge preservation for phantom measurements in 2D and 3D. Furthermore, we discuss the visual results of real clinical data. Finally Section 6 concludes our work.
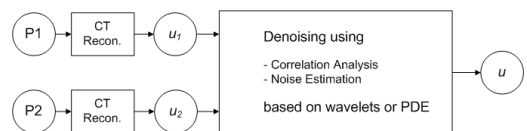
2 Method Overview

Figure 1: Overview of the noise reduction method

Figure 1 shows a brief overview of the denoising methodology: first, two CT datasets u_1 and u_2 are generated, which only differ with respect to noise. Note that if more than two sets are used, the SNR in the separately reconstructed images decreases what leads to a worse edge detection.

In CT, this can be achieved by separate reconstructions from disjoint subsets of projections P1 $\subset$ P and P2 $\subset$ P, with P1 $\cap$ P2 $= \emptyset$. Assuming that the sampling rate is high enough for both single sets of projections (see [9, 10]), then $R\{P\} = 0.5\,(R\{P1\} + R\{P2\})$, with R defining an arbitrary reconstruction operator. Specifically, we reconstruct one dataset from the even and the other from the odd numbered projections using the weighted filtered back projection (WFBP) [11]. Instead of just averaging u_1 and u_2 we use these two datasets as input to our denoising algorithm, which can be a wavelet based or PDE based method.

Both methods have in common that they try to separate structure and noise by taking into account the local correlation of the two input datasets. Additionally, the local standard deviation of noise can be estimated from the difference between u_1 and u_2. After denoising, we obtain u, which corresponds to the reconstruction from the complete set of projections, but with improved signal-to-noise ratio.

3 Wavelet Based Denoising

The discrete, dyadic wavelet transformation (DWT) of a signal is a linear operation that maps the discrete d-dimensional input signal with N sample points onto the set of N wavelet coefficients: $a(\mathbf{x})$ defining the approximation and $w^D(\mathbf{x})$ the detail coefficients at position $\mathbf{x} = (x_1, ..., x_d)$ and orientation D. For the 2D case, e.g., we have $D \in \{LH, HL, HH\}$ altogether resulting in four blocks of coefficients: the lowpass filtered approximation and three detail images which include high frequency structures in the horizontal (LH), vertical (HL) and diagonal (HH) directions, respectively, together with noise in the corresponding frequency band.

Multidimensional signals are usually decomposed by applying a 1D transformation successively to all dimensions, whereas the 1D transformation can be described by a filter bank [12]: The signal is filtered with a high-pass filter $\tilde{g}$ and a corresponding lowpass filter $\tilde{h}$ followed by a dyadic downsampling step respectively. This decomposition can be repeated for the lowpass filtered approximation coefficients until the maximum decomposition level $l_{\max} \leq \log_2 N$ (assumed N is a power of two) is reached leading to a multiresolution decomposition. For perfect reconstruction of the signal, the dual filters g and h are applied to the coefficients at decomposition level l after upsampling. The two resulting parts are summed up leading to the approximation coefficients at level $l - 1$.

The two separately reconstructed datasets u_1 and u_2 are both decomposed into multiple frequency bands and orientations by a discrete dyadic wavelet transformation. Because of the linearity of the wavelet transformation the average of u_1 and u_2 can directly be computed in the wavelet domain. The denoising is performed by applying adapted weights to the averaged high frequency detail coefficients. These weights depend on the local and frequency dependent similarity of the input datasets. Different methods for detecting correlated structures between the two datasets have been proposed in [4]. Here, we use the correlation between the approximation coefficients for the detection of structures. At each decomposition level l for each position $\mathbf{x}$, the empirical correlation coefficients between pixel regions taken from the approximation at level $l - 1$ are computed. The pixel regions in the approximation are chosen within a local neighborhood $\Omega_{\mathbf{x}}$ around the corresponding position $\mathbf{x}^{l-1}$ of $\mathbf{x}^l$:

$$r^l(\mathbf{x}) = \frac{\mathrm{Cov}(a_1^{l-1}, a_2^{l-1})}{\sqrt{\mathrm{Var}(a_1^{l-1})\mathrm{Var}(a_2^{l-1})}} \qquad (1)$$

with

$$\mathrm{Var}(s) = \sum_{\tilde{\mathbf{x}} \in \Omega_{\mathbf{x}}} (s(\tilde{\mathbf{x}}) - \bar{s})^2 \qquad (2)$$

and

$$\mathrm{Cov}(s_1, s_2) = \sum_{\tilde{\mathbf{x}} \in \Omega_{\mathbf{x}}} (s_1(\tilde{\mathbf{x}}) - \bar{s}_1)(s_2(\tilde{\mathbf{x}}) - \bar{s}_2),$$
$$(3)$$

where a_1^{l-1} and a_2^{l-1} define the approximation coefficients of u_1 and u_2, respectively, $\bar{a}_1^{l-1}$ and $\bar{a}_2^{l-1}$ denote the corresponding average values within $\Omega_{\mathbf{x}}$. The neighborhood $\Omega_{\mathbf{x}}$ is chosen in dependence on the used wavelet in order to assure that all pixels that influenced the detail coefficient at position $\mathbf{x}$ during decomposition and all those coefficients that are influenced by the reconstruction from this

coefficient are included into the correlation analysis. Therefore, the neighborhood is defined by the length of the used analysis ($\tilde{g}$, $\tilde{h}$) and synthesis (g and h) filters. If we assume that the length $\mathbf{m} = (m_1, \ldots, m_d)$ of all these four filters is the same and even, we define

$$\Omega_{\mathbf{x}} = \left\{ \tilde{\mathbf{x}}^{l-1} \,\middle|\, |\tilde{x}^{l-1} - x^{l-1}| \leq \mathbf{m} \right\}. \quad (4)$$

The final noise suppressed result u is computed by an inverse wavelet transformation from the averaged and weighted coefficients:

$$a^{l_{\max}}(\mathbf{x}) = \frac{1}{2}\left(a_1^{l_{\max}}(\mathbf{x}) + a_2^{l_{\max}}(\mathbf{x}) \right), \quad (5)$$

$$w^{D,l}(\mathbf{x}) = \frac{1}{2}\left(w_1^{D,l}(\mathbf{x}) + w_2^{D,l}(\mathbf{x}) \right) f^l(\mathbf{x}),$$
$$l \in \{1, \ldots, l_{\max}\},$$

with weighting function

$$f^l(\mathbf{x}) = \frac{1}{2}\left(r^l(\mathbf{x}) + 1 \right). \quad (6)$$

4 PDE Based Denoising

4.1 PDE model

In contrast to the wavelet based denoising the PDE based denoising works in the spatial domain. Noise is removed using a nonlinear diffusion process described by the nonlinear PDE

$$u - u^0 = \tau \mathrm{div}(g(\|\nabla u\|)\nabla u) \quad (7)$$

with Neumann boundary conditions. This is equivalent to solving a Perona and Malik nonlinear isotropic diffusion equation [7] for a fixed artificial time step τ. The initial image u^0 is set to the average of the two input images u_1^0 and u_2^0. The edge-stopping function $g(\|\nabla u\|)$ regulates the diffusion process. We use the Tukey edge-stopping function

$$g_\sigma(x) = \begin{cases} \left(1 - \left(\frac{x}{\sigma}\right)^2\right)^2, & |x| \leq \sigma, \\ 0, & |x| > \sigma. \end{cases} \quad (8)$$

introduced in [13] because of its good edge preserving properties. Usually, the parameter σ is set to the standard deviation when dealing with white noise.

For denoising CT images we have to modify g_σ resulting in $\tilde{g}_V$ described next (cf. (15)) to achieve adequate results and we simultaneously denoise the two input CT images u_1^0 and u_2^0 and its average u^0.

This means we have to solve the nonlinear system of partial differential equations

$$u - u^0 = \tau \mathrm{div}(D'_{u_1,u_2}\nabla u) \quad (9a)$$
$$u_1 - u_1^0 = \tau \mathrm{div}(D'_{u_1,u_2}\nabla u_1) \quad (9b)$$
$$u_2 - u_2^0 = \tau \mathrm{div}(D'_{u_1,u_2}\nabla u_2) \quad (9c)$$

with Neumann boundary conditions. Here, D'_{u_1,u_2} is a nonlinear diffusion tensor with

$$D'_{u_1,u_2} = \tilde{g}_V \cdot E \quad (10)$$

in the isotropic case and

$$D'_{u_1,u_2} = \tilde{g}_V(D) \quad (11)$$

with $D = 0.25\left((\nabla u_1 + \nabla u_2)(\nabla u_1 + \nabla u_2)^T \right)$ in the anisotropic case. E denotes the identity matrix and $\tilde{g}_V$ is applied, e.g., in the 2D case, to D by applying $\tilde{g}_V$ to the eigenvalues λ_1, λ_2 of D and leaving the eigenvectors v_1, v_2 of D unchanged, i.e., $D'_{u_1,u_2} = \tilde{g}_V(\lambda_1)v_1 v_1^T + \tilde{g}_V(\lambda_2)v_2 v_2^T$.

Two ways of exploiting the availability of two input images with uncorrelated noise are to compute the correlation between both and to estimate noise variance.

Because of the spatially varying noise properties in CT images the analysis is done locally in a neighborhood $\Omega_{\mathbf{x}}$ around a pixel $\mathbf{x}$ analog to wavelet based denoising. Additionally, the neighboring pixels $\tilde{\mathbf{x}}$ are weighted with Gaussian weights

$$\alpha(\tilde{\mathbf{x}}, \mathbf{x}) = \frac{1}{\sigma\sqrt{2\pi}}\left(-\frac{1}{2}e^{\frac{\|\tilde{\mathbf{x}} - \mathbf{x}\|^2}{\sigma^2}} \right) \quad (12)$$

depending on the distance between pixel $\tilde{\mathbf{x}}$ and $\mathbf{x}$. A local estimate for the correlation of two image regions can be computed by the weighted correlation coefficient

$$c_\alpha(\mathbf{x}) = \frac{\mathrm{Cov}_\alpha(u_1, u_2)}{\sqrt{\mathrm{Var}_\alpha(u_1)\mathrm{Var}_\alpha(u_2)}}.$$

using the weighted covariance

$$\mathrm{Cov}_\alpha(s_1, s_2) = \sum_{\tilde{\mathbf{x}} \in \Omega_{\mathbf{x}}} \prod_{j=1}^{2}(s_j(\tilde{\mathbf{x}}) - \bar{s}_j)\alpha(\tilde{\mathbf{x}}, \mathbf{x})$$

and weighted variance

$$\mathrm{Var}_\alpha(s) = \sum_{\tilde{\mathbf{x}} \in \Omega_{\mathbf{x}}} (s(\tilde{\mathbf{x}}) - \bar{s})^2\alpha(\tilde{\mathbf{x}}, \mathbf{x}),$$

where $\bar{s}$ is the local gray value average. Because in our case only the amount of similarity between image regions is interesting, the values below 0 of c_α, denoting anti-correlation, are set to 0, yielding a local similarity measure

$$C_\alpha(\mathbf{x}) = \begin{cases} 1 & c_\alpha(\mathbf{x}) > 0 \\ 0 & c_\alpha(\mathbf{x}) \leq 0 \end{cases}. \qquad (13)$$

A visualization of C_α of the input images of a liver CT scan is shown in Fig. 2(a).

Two input images give us the possibility to estimate the local noise variance of the average of the input images by [14]

$$V(\mathbf{x}) = \frac{\displaystyle\sum_{\tilde{\mathbf{x}} \in \Omega_{\mathbf{x}}} \alpha(\tilde{\mathbf{x}}, \mathbf{x})(u_1(\tilde{\mathbf{x}}) - u_2(\tilde{\mathbf{x}}))^2}{4 \displaystyle\sum_{\tilde{\mathbf{x}} \in \Omega_{\mathbf{x}}} \alpha(\tilde{\mathbf{x}}, \mathbf{x})}. \qquad (14)$$

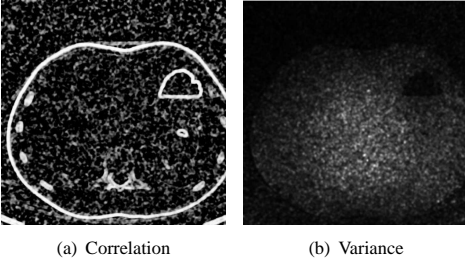A plot of the estimated local variance V in Fig. 2(b) shows the spatially changing behavior of the noise variance.

(a) Correlation   (b) Variance

Figure 2: Plot of the local correlation C_α and local variance estimate V of a liver CT scan.

Based on the Tukey edge-stopping function we now design a new function taking into account V and C_α. The fixed parameter for the noise standard deviation of the Tukey edge-stopping function is replaced by $V(\mathbf{x})$ resulting in

$$\tilde{g}_V(x) = \begin{cases} \left(1 - \frac{x^2}{V(\mathbf{x})}\right)^2, & |x| \leq \beta\sqrt{V(\mathbf{x})}, \\ 0, & |x| > \beta\sqrt{V(\mathbf{x})}. \end{cases} \qquad (15)$$

with an additional fixed weighting factor $\beta \in \mathbb{R}^+$. If nothing else is stated, we set $\beta = 1$.

The square root of the product of the gradients on the input images

$$\|\nabla u_{1,2}\| = \sqrt{\|\nabla u_1\| \cdot \|\nabla u_2\|} \qquad (16)$$

is taken as input for the edge-stopping function $\tilde{g}_V$. It is further linearly scaled by the local similarity measure, i.e., we use $\tilde{g}_V(s), s \in \mathbb{R}$ with

$$s = \begin{cases} \|\nabla u_{1,2}\| \cdot W(\mathbf{x}) & \text{if } W(\mathbf{x}) > 0, \\ 0 & \text{else} \end{cases} \qquad (17)$$

and

$$W(\mathbf{x}) = 1 + \gamma(2C_\alpha(\mathbf{x}) - 1) \qquad (18)$$

with $\gamma \in \mathbb{R}^+$. This has the effect to damp high gradients in image regions with small similarity, e.g., in homogeneous regions, and to enlarge the gradient where similarity is high, i.e., when image structure is present.

4.2 PDE solver

We discretize Eq. (9) in 2D and 3D by finite volumes on a cell-based grid Ω^h, the gradients required for the computation of $\tilde{g}_V$ are approximated by finite differences. The resulting nonlinear system of equations

$$A^h(u^h) = f^h \qquad (19)$$

is solved by a cell-based nonlinear multigrid solver on a hierarchy of grids [15, 16, 17, 18] based on the full approximation scheme (FAS) [19] to obtain the denoised discrete image u^h. In the following explanations, we restrict ourselves to two grids for simplicity, a fine grid Ω^h and a coarse grid Ω^H.

To deal with the nonlinearity we apply an inexact lagged diffusivity [20, 21]. The idea is to keep the diffusivity function $\tilde{g}_V(s)$ constant during the iteration step $k + 1$ and to evaluate it at the old iteration step k. That means we successively solve

$$u^{k+1} - u_0 = \tau \text{div}\left(\left(D'_{u_1,u_2}\right)^k \nabla u^{k+1}\right) \qquad (20a)$$

$$u_1^{k+1} - u_1^0 = \tau \text{div}\left(\left(D'_{u_1,u_2}\right)^k \nabla u_1^{k+1}\right) \qquad (20b)$$

$$u_2^{k+1} - u_2^0 = \tau \text{div}\left(\left(D'_{u_1,u_2}\right)^k \nabla u_2^{k+1}\right) \qquad (20c)$$

Note that now the three solution components u, u_1, and u_2 are decoupled and can be updated independently from each other.

Within the FAS multigrid iteration the Gauss-Seidel method denoted by the operator S^ν, where ν are the number of Gauss-Seidel iterations, serves as pre- and post-smoother. After each Gauss-Seidel iteration on each level, we update the values of the diffusivity function $\tilde{g}_V(s)$. Furthermore, we apply simple restriction and interpolation operators [16].

The restriction operator in 2D can be described by the stencil

$$I_h^H = \frac{1}{4} \begin{bmatrix} 1 & & 1 \\ & \cdot & \\ 1 & & 1 \end{bmatrix}, \qquad (21)$$

where the dot in the stencil denotes the position on the coarse grid at which the restriction is applied, and the constant interpolation in 2D by the stencil

$$I_H^h = \begin{bmatrix} 1 & & 1 \\ & \cdot & \\ 1 & & 1 \end{bmatrix}. \qquad (22)$$

Extension to 3D is straightforward. We denote one FAS iteration, e.g., by FAS(2,2), i.e., we perform 2 pre- and 2 post-smoothing steps. For the results in the next section we typically apply 3-4 FAS(2,2) iterations.

The FAS scheme can be extended to full multigrid (FMG) by constructing an image pyramid and starting to compute a denoised image at the lowest resolution or level. Then, the solution is interpolated to the next finer level and used as an initial guess there. On each level one or more FAS iterations are computed. One recursive FAS iterations to solve the nonlinear system $A^h u^h = f^h$ is shown in Algorithm 1. The initial guess $u_h^{(0)} = 0$.

5   Comparison Results

For a thin reconstructed example slice (0.8 mm) of an abdomen CT scan (see Fig.3), Fig. 4 shows the results for the proposed method in comparison to one standard nonlinear diffusion method and the wavelet based approach.
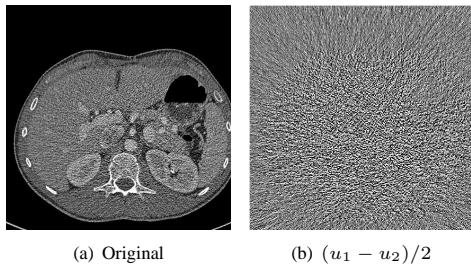

(a) Original   (b) $(u_1 - u_2)/2$

Figure 3: Original average image and its difference images (one slice is of size 512×512), displayed with $c = 0$ and $w = 200$.

In 2D we used the redundant SWT, in 3D the non-redundant DWT, both in combination with the Haar wavelet and three decomposition levels. The noise reduced images are compared to the average of the input images, which corresponds to the result of a reconstruction from all projections and is in the following referred to as the original image. In Fig. 5 the corresponding difference images to the original image are shown, providing an impression of the denoising behavior of the different approaches. Fig. 4(a) clearly demonstrates that a standard nonlinear diffusion method fails to denoise a CT image with spatially varying noise power in an adequate manner. While noise in the center of the image is nearly unchanged, the outer regions are already blurred. Using the proposed PDE approach or the wavelet based method (Fig. 4(c)- 4(f)) shows that both methods are capable of adapting themselves to the local noise variance, thus removing noise more uniformly. For both approaches in 2D a noise reduction of about 45% is achieved throughout the image. To get a proper estimate of the correlation of the input images a 5×5 neighborhood was used in the wavelet approach and a 8×8 neighbourhood with gaussian weights of standard deviation 2 in case of the PDEs. Because image structures like edges have influence on the correlation value of distant pixels in their neighborhood, unfortunately noise remains around high contrast edges if the window for correlation analysis is chosen too large. However, if the window is chosen too small the correlation analysis gets unreliable. Using 3D data reduces this problem, because pixels for estimating the noise variance and correlation can be taken from the neighborhood in all three dimensions. Fig. 4(d) and 4(f) show the results in 3D using a window of $5 \times 5 \times 5$ pixels (with gaussian weights of standart derivation 1 in case of the PDEs). It can be seen clearly that a strong noise suppression of about 60% is achieved while image structures are well preserved.

These images were also used for clinical tests, where a radiologist judged the images with respect to noise and visibility of structures in two consecutive tests. Within these tests unlabeled image pairs were shown to the radiologist in randomized order. For all image pairs, the radiologist decided if there was one preferred image with respect to the current evaluation criterion. Switching the position of the two images, allowed to notice even small dif-

Algorithm 1 FAS iteration (V-cycle): Compute $u_h^{(k+1)} = M_h^{FAS}\left(u_h^{(k)}, A^h, f^h, \nu_1, \nu_2\right)$

1: $\bar{u}_h^{(k)} = S_h^{\nu_1}\left(u_h^{(k)}, A^h, f^h\right)$ {pre-smoothing}

2: $r^h = f^h - A^h\left(\bar{u}_h^{(k)}\right)$ {compute residual}

3: $r^H = \mathcal{I}_h^H r^h$ {restrict residual}

4: $\bar{u}^H = \mathcal{I}_h^H \bar{u}_h^{(k)}$ {restrict solution}

5: $f^H = r^H + A^H\left(\bar{u}^H\right)$

6: **if** number of coarse grid points $< \epsilon_{min}$ **then**

7:     Solve nonlinear problem $A^H(w^H) = f^H$ by a suitable nonlinear solver or sufficiently many Gauss-Seidel iterations

8: **else**

9:     $w^H = M_H^{FAS}\left(\bar{u}^H, A^H, f^H, \nu_1, \nu_2\right)$

10: **end if**

11: $e^H = w^H - \bar{u}^H$

12: $e^h = \mathcal{I}_H^h e^H$ {interpolate error}

13: $\tilde{u}_h^{(k)} = \bar{u}_h^{(k)} + e^h$ {coarse grid correction}

14: $u_h^{(k+1)} = S_h^{\nu_2}\left(\tilde{u}_h^{(k)}, A^h, f^h\right)$ {post-smoothing}

---

ferences between the images. Within the tests all denoised images were compared to the original image. Furthermore, the 2D and 3D results of the proposed PDE approach were compared to the results of the wavelet based approach. Summarizing, the test showed that all denoised images were judged superior in comparison to the original for both evaluation criteria.

For the comparison between PDE and wavelets the results of the tests were not that clear. With respect to noise the wavelet based methods were preferred. Regarding the visibility of structures the PDE approach gives better results.

In addition to the visual inspection, quantitative tests were performed evaluating noise reduction and edge preservation in phantom images. For generating the simulated CT-scans the *DRASIM* software package provided by Karl Stierstorfer [22] was used. The phantom consists of a water cylinder with an inlaid quartered cylinder of defined density. In order to test the preservation of edges at different contrast-to-noise levels the density of the object was varied leading to edge-contrasts between 20 to 100 Hounsfield units (HU). The Hounsfield scale is a quantitative measure for radiodensity, i.e., it describes the relative transparency of a material, if X-rays pass through it.

In addition to noisy phantoms, ideal CT-scans were simulated leading to noise-free ground-truth

data. In CT a standard measurement for resolution is the modulation transfer function (MTF) (see e.g. [10, 23]), indicating how many line pairs per cm (lp/cm) can be distinguished. It is possible to determine the local MTF directly from the edge in an image. For this purpose, we manually selected a fixed region of 20×125 pixels around an edge (with a slope of approx. 4 degrees). The slight tilt of the edge allows a higher sampling of the edge profile, which is additionally averaged along the edge. The derivation of the edge profile leads to the line-spread function (LSF). The Fourier transformation of the LSF results in the MTF, which is additionally normalized so that $\mathrm{MTF}(0) = 1$. Reliable measurements of the MTF from this *edge technique* can only be achieved if the contrast of the edge is much higher than the pixel noise in the images [24].

In case of the wavelet based approach this can be easily circumvented by applying the computed weights at each decomposition level to the wavelet coefficients of the ideal noise-free image and computing the inverse transformation. This has the effect of making the influence of the weighting to the real signal directly visible. The MTF can then be computed at the edge in the processed noise-free image.

In case of the diffusion method this is not possible and, therefore, the average of 200 denoised slices was used for computing the MTF. The MTFs

(a) Tukey - Original   (b) 2D Anisotropic - Original

(c) 2D Isotropic - Original   (d) 3D Isotropic - Original

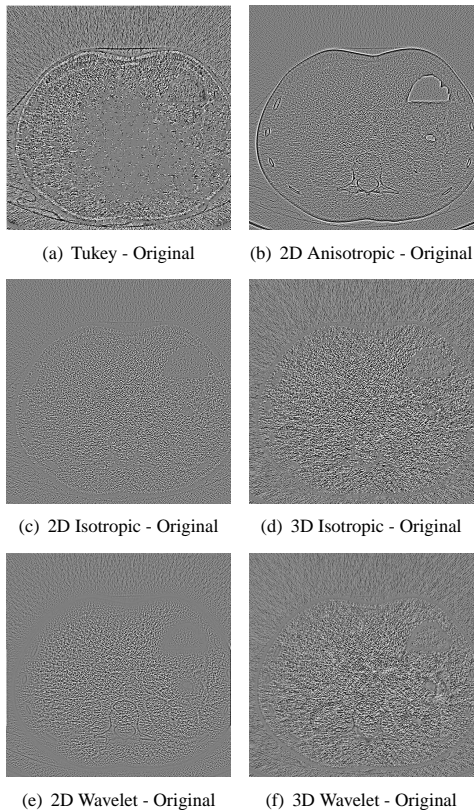(e) 2D Wavelet - Original   (f) 3D Wavelet - Original

Figure 5: Difference images, displayed with $c = 0$ and $w = 200$.

measured at edges with different contrasts are plotted in Fig. 6 and compared to the MTF measured at the original edge of 100 HU. All approaches used a 5×5 neighborhood, the PDE with Gaussian weights of standard derivation 1.

It can be clearly seen that the preservation of an edge very much depends on the contrast-to-noise level. The lower the contrast at the edge the stronger the MTF falls below the original curve, indicating that the edge was blurred. Fig. 6(a) shows that the phantom edges with a contrast of more than 40 HU are nearly fully preserved by the 2D PDE method. Additionally, due to the large time parameter needed to obtain a noise reduction of 45% the edge is enhanced by the diffusion process. The 3D PDE approach leads to better results for low-contrasty edges and the amount of sharpening applied is lower, as it can be seen in Fig. 6(c). Suppris-

ingly, if anisotropic diffusion is used the edges are blurred as Fig. 6(b) shows. It seems that this approach is not capable of denoising images with fine structures, because even minor errors in the estimation of the edge gradient lead to a blurring over it.

For comparing the PDE approach to the wavelet based method the ρ_{50}-values of the MTFs were plotted against the contrast of the edge in Fig. 7. The ρ_{50}-value is defined as $\mathrm{MTF}(\rho_{50}) = 0.5$. Additionally, the values of the original noise-free images are plotted for comparison. It can be seen that the edge preservation of the PDE method outperforms the wavelet based method.

6 Conclusions

Isotropic and Anisotropic diffusion is adapted to be able to deal with the special noise characteristics of CT data. The diffusion depends on local noise variations and an estimation of the real image structure by calculating correlations between two input images with uncorrelated noise. The approach is compared to a similar wavelet based denoising method.

To enable the use of the presented algorithms in practical applications, it is necessary to improve their performance. Currently it takes for both approaches on a Laptop (Pentium M 2.0 GHz and 1 GB RAM) and typical parameter settings about 3–7 seconds to denoise a 2D slice of size 512×512 and about 80–120 seconds for a 3D volume of size $512 \times 512 \times 16$. Although the wavelet method is implemented within Matlab, it is slightly faster. The PDE based approach is implemented in C++. Applying standard optimization techniques [25, 26, 27] to the unoptimized multigrid solver could lead to a performance gain of factor 2–5.

References

[1] J. Hsieh, "Adaptive streak artifact reduction in computed tomography resulting from excessive x-ray photon noise," *Medical Physics*, vol. 25, no. 11, pp. 2139–2147, November 1998.

[2] M. Kachelrieß, O. Watzke, and W. A. Kalender, "Generalized multi-dimensional adaptive filtering for conventional and spiral single-slice, multi-slice, and cone-beam CT," *Medical Physics*, vol. 28, no. 4, pp. 475–490, 2001.
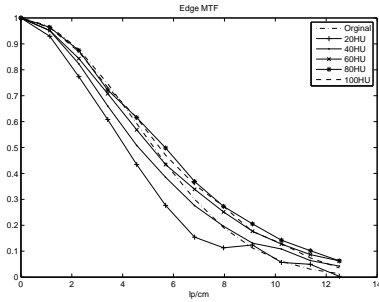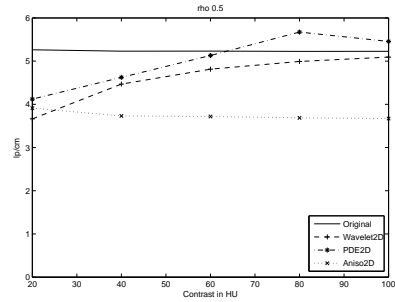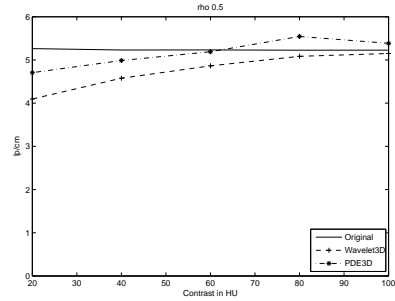
(a) 2D Isotropic
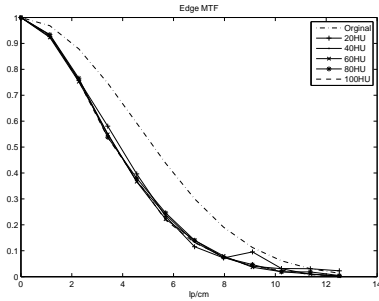
(b) 2D Anisotropic
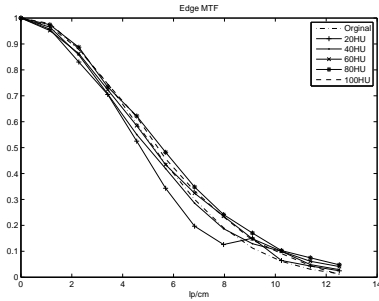
(c) 3D PDE

Figure 6: MTFs achieved with the PDE approach in 2D and 3D for different contrasts at the edge.

(a) 2D PDE vs. Wavelet

(b) 3D PDE vs. Wavelet

Figure 7: Comparison of ρ_{50}-values achieved for PDE or wavelet based method plotted against the contrast of the edge.

[3] O. Demirkaya, "Reduction of noise and image artifacts in computed tomography by nonlinear filtration of projection images," in *Proc. SPIE, Medical Imaging 2001: Image Processing*, M. Sonka and K. M. Hanson, Eds., vol. 4322, 2001, pp. 917–923.

[4] A. Borsdorf, R. Raupach, and J. Hornegger, "Wavelet based Noise Reduction by Identification of Correlation," in *Pattern Recognition (DAGM 2006), Lecture Notes in Computer Science*, K. Franke, K. Müller, B. Nickolay, and R. Schäfer, Eds., vol. 4174. Berlin: Springer, 2006, pp. 21–30.

[5] A. Borsdorf, R. Raupach, and J. Hornegger, "Separate CT-Reconstruction for Orientation and Position Adaptive Wavelet Denoising," in *Bildverarbeitung für die Medizin 2007*, A. Horsch, T. Deserno, H. Handels, H. Meinzer, and T. Tolxdoff, Eds. Berlin: Springer, 2007, pp. 232–236.

[6] M. Mayer, A. Borsdorf, H. Köstler, J. Hornegger, and U. Rüde, "Nonlinear Diffusion Noise Reduction in CT Using Correlation Analysis," in *3rd Russian-Bavarian Conference on Biomedical Engineering*, J. Hornegger, E. Mayr, S. Schookin, H. Feußner, N. Navab, Y. Gulyaev, K. Höller, and V. Ganzha, Eds., vol. 1. Erlangen, Germany: Union aktuell,

2007, pp. 155–159.

[7] P. Perona and J. Malik, "Scale-space and edge detection using anisotropic diffusion," *IEEE Trans. Pattern Anal. Mach. Intell.*, vol. 12, no. 7, pp. 629–639, 1990.

[8] J. Weickert, *Anisotropic Diffusion in Image Processing*. Teubner Verlag, Stuttgart, Germany, 1998.

[9] A. Kak and M. Slanely, *Principles of Computerized Tomographic Imaging*. Society for Industrial and Applied Mathematics, Juli 2001, http://www.slaney.org/pct/pct-toc.html.

[10] T. Buzug, *Einführung in die Computertomographie*. Berlin Heidelberg: Springer-Verlag, 2004.

[11] K. Stierstorfer, A. Rauscher, J. Boese, H. Bruder, S. Schaller, and T. Flohr, "Weighted FBP - a simple approximate 3DFBP algorithm for multislice spiral CT with good dose usage for arbitrary pitch," *Physics in Medicine and Biology*, vol. 49, no. 11, pp. 2209–2218, 2004.

[12] G. Strang and T. Nguyen, *Wavelets and Filter Banks*. Wellesley- Cambridge Press, 1996.

[13] M. J. Black, G. Sapiro, D. Marimont, and D. Heeger, "Robust anisotropic diffusion," *IEEE Trans. on Image Processing*, vol. 7, no. 3, pp. 421–432, 1998.

[14] A. Borsdorf, R. Raupach, and J. Hornegger, "Separate CT-Reconstruction for Orientation and Position Adaptive Wavelet Denoising," in *Bildverarbeitung für die Medizin 2007*, A. Horsch, T. Deserno, H. Handels, H. Meinzer, and T. Tolxdoff, Eds. Springer-Verlag, Berlin, Heidelberg, New York, 2007, pp. 232–236.

[15] U. Trottenberg, C. Oosterlee, and A. Schüller, *Multigrid*. Academic Press, San Diego, CA, USA, 2001.

[16] P. Wesseling, *Multigrid Methods*. Edwards, Philadelphia, PA, USA, 2004.

[17] E. Kalmoun, H. Köstler and U. Rüde, "3D optical flow computation using a parallel variational multigrid scheme with application to cardiac C-arm CT motion," *Image and Vision Computing*, vol. 25, no. 9, pp. 1482–1494, 2007.

[18] A. Bruhn, "Variational optic flow computation: Accurate modeling and efficient numerics," Ph.D. dissertation, Department of Mathematics, Saarland University, Saarbrücken, Germany, 2006.

[19] A. Brandt, "Multi-Level Adaptive Solutions to Boundary-Value Problems," *Mathematics of Computation*, vol. 31, no. 138, pp. 333–390, 1977.

[20] T. Chan and P. Mulet, "On the convergence of the lagged diffusivity fixed point method in total variation image restoration," *SIAM Journal on Numerical Analysis*, vol. 36, no. 2, pp. 354–367, 1999.

[21] C. Vogel, *Computational Methods for Inverse Problems*. Society for Industrial and Applied Mathematics (SIAM), Philadelphia, PA, USA, 2002.

[22] K. Stierstorfer, T. Flohr, and H. Bruder, "Segmented multiple plane reconstruction: A novel approximate reconstruction scheme for multi-slice spiral CT," *Physics in Medicine and Biology*, vol. 47, no. 4, pp. 2571–2581, July 2002.

[23] O. Dössel, *Bildgebende Verfahren in der Medizin: Von der Technik zur medizinischen Anwendung*. Springer-Verlag, Berlin, Heidelberg, New York, 1999.

[24] I. A. Cunningham and B. K. Reid, "Signal and noise in modulation transfer function determinations using the slit, wire, and edge techniques," *Medical Physics*, vol. 19, no. 4, pp. 1037–1044, July 1992.

[25] C. Douglas, J. Hu, M. Kowarschik, U. Rüde, and C. Weiß, "Cache Optimization for Structured and Unstructured Grid Multigrid," *Electronic Transactions on Numerical Analysis (ETNA)*, vol. 10, pp. 21–40, 2000.

[26] H. Köstler, M. Stürmer, and U. Rüde, "A fast full multigrid solver for applications in image processing," Department of Computer Science 10 (System Simulation), Friedrich-Alexander-University of Erlangen-Nuremberg, Germany, Tech. Rep. 07-6, 2007, submitted to Numerical Linear Algebra with Applications.

[27] C. Weiß, "Data Locality Optimizations for Multigrid Methods on Structured Grids," Ph.D. dissertation, Lehrstuhl für Rechnertechnik und Rechnerorganisation, Institut für Informatik, Technische Universität München, Germany, 2001.

(a) Tukey

(b) 2D Anisotropic

(c) 2D Isotropic

(d) 3D Isotropic

(e) 2D Wavelet

(f) 3D Wavelet

Figure 4: Denoising results for a CTA of a liver, displayed with $c = 200$ and $w = 700$.